Reprinted from

JAPANESE JOURNAL OF
APPLIED
PHYSICS

REGULAR PAPER

Myocardial Strain Imaging with High-Performance Adaptive Dynamic Grid Interpolation Method

Shuhui Bu, Makoto Yamakawa, and Tsuyoshi Shiina

Jpn. J. Appl. Phys. **49** (2010) 07HF25

Japanese Journal of Applied Physics **49** (2010) 07HF25 **REGULAR PAPER**

Myocardial Strain Imaging with High-Performance Adaptive Dynamic Grid Interpolation Method

Shuhui Bu, Makoto Yamakawa[1], and Tsuyoshi Shiina

Human Health Science, Graduate School of Medicine, Kyoto University, Kawara-machi, Shogoin, Sakyo-ku, Kyoto 606-8507, Japan
[1]*Advanced Biomedical Engineering Research Unit, Kyoto University, Kawara-machi, Shogoin, Sakyo-ku, Kyoto 606-8507, Japan*

Received November 18, 2009; accepted February 17, 2010; published online July 20, 2010

The accurate assessment of local myocardial strain is important for diagnosing ischemic heart diseases because decreased myocardial motion often appears in the early stage. Calculating the spatial derivation of displacement is a necessary step in the strain calculation, but the numerical calculation is extremely sensitive to noise. Commonly used smoothing methods are the moving-average and median filters; however, these methods have a trade-off between spatial resolution and accuracy. A novel smoothing/fitting method is proposed for overcoming this problem. In this method, the detected displacement vectors are discretized at mesh nodes, and virtual springs are connected between adjacent nodes. By controlling the elasticity of the virtual springs, misdetected displacements are fitted without the above problem. Further improvements can be achieved by applying a Kalman filter for position tracking, and then calculating the strain from the accumulated displacement vectors. From the simulation results, we conclude that the proposed method improves the accuracy and spatial resolution of the strain images.

DOI: 10.1143/JJAP.49.07HF25

1. Introduction

One of the aims in cardiac imaging and image analysis is to assess the regional kinematic functions of the left ventricle (LV) of the heart. From these regional functions, quantitative estimates of the location and extent of ischemic myocardial injury can be obtained. Regional left ventricular deformation can be determined using the principal imaging modalities, including echocardiography, radionuclide imaging, computed tomography, and magnetic resonance imaging (MRI).

MRI tagging is regarded as a reference method for the assessment of LV deformation, because it can provide angle-independent three-dimensional (3D) motion of the heart muscle over time, whereas with other imaging methods, tracking is usually limited to the shape of the inner and outer contours of the heart wall. Typically, only 2–3 tagging lines can be obtained within the myocardium; therefore, its spatial resolution is low although the accuracy of estimated displacements at tracking points is high. In addition to its low spatial resolution, MRI tagging is limited by its shortcomings of low frame-rate, high cost, and time-consuming.

Compared with MRI tagging, echocardiography has the advantages of high frame-rate, high spatial resolution, and low cost. The widely applied echocardiography methods for cardiac imaging are B-mode imaging, M-mode imaging, tissue Doppler imaging (TDI),[1–4] and strain-rate imaging (SRI).[5–7] The ventricle shape can be visualized by B-mode imaging, but quantitative information on motion is difficult to analyze. Through M-mode imaging, the myocardial motion of a specified scan line can be visualized within a certain period, but motion information can only be obtained in the beam direction. TDI and SRI also only provide motion information in the beam direction.[8] Furthermore, if the range of motion is larger than one-quarter of a wavelength, aliasing may occur, precluding accurate myocardial strain measurement.

To overcome the limitation of angle dependence in echocardiography, two types of studies have been performed: cardiac motion analysis and speckle-tracking echocardiography (STE). The cardiac motion analysis methodology uses various medical images as sources, and incorporates a constrained model for fitting the results. For example, Papademetris *et al.* proposed a method[9] by which myocardial boundaries are extracted from B-mode images. Then the myocardial strain tensors are calculated by applying the finite element method (FEM). However, this method uses segmentation results, therefore, the spatial resolution is low. STE[6,10–12] provides another way of tracking motion in ultrasound. This method provides the myocardial tissue velocity, strain, and strain rate, independent of the cardiac translation and beam angle. However, one type of STE[10,11] is based on the speckle tracking or image registration of B-mode images. However the spatial resolution of B-mode images is much lower than that of raw RF data, therefore the spatial resolution is not very perfect. Another type of STE[6,12] is based on the tracking of RF data. Because the tracking of RF data is sensitive to noise, a smoothing filter must be applied before the strain calculation.

In recent years, novel lateral modulation methods[13,14] for high-spatial-resolution 2D displacement estimation have been researched. At a high spatial resolution, strain calculation is sensitive to noise. Conventional smoothing filters suffer from a critical drawback: there is a trade-off between spatial resolution and accuracy. To overcome this problem, the previously proposed dynamic grid interpolation[15] has been extended so that the smoothing effect can be adjusted adaptively; this method is called adaptive dynamic grid interpolation (ADGI), and considers mechanical relationships in the imaging model. Conventional myocardial TDI and SRI imaging systems seldom consider the myocardial mechanical model, and cardiac motion analysis methods seldom use high-accuracy displacement data. Our proposed method combines the advantages of the two methods, simultaneously achieving high spatial resolution and accuracy. In our other study,[16] this displacement-smoothing filter is applied to tissue strain imaging, and the results were promising.

Usually, when the scanning frame rate is high, the correlation coefficient, which is calculated from autocorrelation or cross-correlation, will be high. However only using the phase-shift data of two consecutive frames, the dynamic

range of the displacements is low. Therefore, the strain calculation will be affected by the high relative noise. In this study, a Kalman filter (KF) is applied to position tracking by which the displacement data of multiple frames can be tracked in the temporal dimension, and the myocardial strain is calculated from the accumulated displacement to improve the accuracy. From the simulation results, we can conclude that our method can provide more accurate myocardial strain images.

The rest of this paper is organized as follows. First in §2 we present the principle of myocardial strain imaging. The simulation models and numerical simulations are described in §3. Then we discuss our overall findings in §4. Finally, the conclusions of our work are provided in §5.

2. Myocardial Strain Imaging

In this method, a 2D array transducer acquires echo data from the myocardium through volumetric sector scanning. RF signals for each scan line are received at all elements in the probe. The phase-shift at every measuring point between two consecutive frames is calculated by the combined autocorrelation method (CAM)[17] or the extended CAM (ECAM),[18,19] and the displacement vectors are calculated by the weighted-phase gradient (WPG) method[20,21] from the obtained phase-shifts. Meanwhile, the myocardial endocardium boundaries are segmented from the B-mode image, for example, an automated segmentation method for the heart wall[22] has been proposed recently. The epicardium boundary is calculated from the endocardium boundary by adding a fixed radius. Next, the myocardium meshes are generated from the myocardial boundaries. The detected displacement vectors and myocardial meshes are then input into a displacement-resampling module. The displacement vectors in each mesh node are calculated by bilinear interpolation,[23] their coordinates are translated from Cartesian coordinates to cylindrical coordinates, and ADGI is then used to fit the displacement vectors. The position vectors of each node are tracked by a KF, and then the displacement vectors are accumulated. Finally, the strain tensors are calculated from the processed displacement vectors.

2.1 Adaptive dynamic grid interpolation

Because of scattering, reflection, and the interference of ultrasound beams in the tissue, there is a lot of noise in ultrasound echo signals. Therefore, the raw signals are rarely used directly in motion tracking. The most commonly used smoothing filters for ultrasound imaging are the moving-average and median filters. These two filters are simple and easy to understand, and easily achieve real-time processing. In myocardial strain imaging, calculating the spatial derivation of displacement is a necessary step in the strain calculation, but this numerical calculation is extremely sensitive to noise, especially when the spatial resolution is high. To obtain high-accuracy and stable strain data, smoothing filters must be applied before the strain calculation. In this situation, the above two filters have the following limitations: (1) A trade-off between spatial resolution and stability. If the window is large, the spatial resolution decreases; if the window is small, the filters cannot handle the speckle noise of a large area, and the fluctuations in the strain images are large. (2) Because the window size is fixed, the smoothing effect is the same in all positions, but the noise amplitude is not uniform. Therefore, it is difficult to select a globally optimized window size. A large window causes a loss of detailed information in regions where the noise amplitude is small. If the window is small, however, it is not stable in high-noise amplitude regions. (3) The moving-average filter simply averages the values of several adjacent nodes, and the smoothing effect is not globally optimized. If the error at a position is large, the values of all neighboring nodes are affected. Although the median filter can remove this type of noise, unlike typical image data, errors in ultrasonic data do not usually appear only at one sampling node. Therefore, the effect of this filter is limited. Under some conditions, even if the window is extremely large, the smoothing effect is also not perfect. (4) The smoothed data from these two filters do not always follow the laws of physics.

The detailed process of ADGI is described as follows. The first step is to create a mesh that represents the region of interest (ROI). In our study, the endocardium boundary is segmented, and the epicardium boundary is calculated from the endocardium boundary by adding a fixed radius. Then the myocardium is divided into quadrilateral elements in the radial and circumferential directions. Virtual springs are connected between adjacent nodes to restrict erroneous motions. Finally, by combining the detected displacement vectors and displacement-revising vectors, high-accurate and high-spatial-resolution displacement vectors can be obtained. An illustration of the mesh definition and displacement vectors is shown in Fig. 1. In ADGI, the end point of the detected displacement vector is not always located at a mesh node. Therefore, the displacement vectors are resampled and mesh nodes are generated by using bilinear interpolation.

In the following descriptions, the meanings of symbols are listed below:

- $\vec{u} = (u_r, u_c)$: detected displacement vector.
- $\vec{\epsilon} = (\epsilon_r, \epsilon_c)$: displacement-revising vector which will be determined by this method.
- $\vec{u}' = (u'_r, u'_c)$: revised displacement vector.
- Subscripts r and c: denote radial direction component and circumferential direction component, respectively.

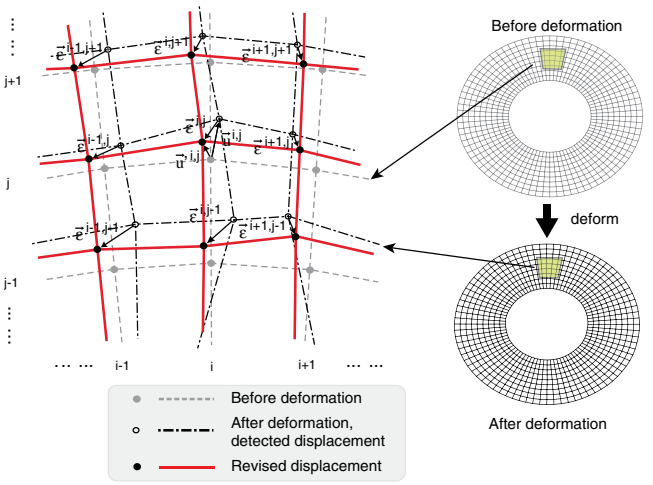

Fig. 1. (Color online) Illustration of mesh definition in the ADGI method and the displacement vectors.

- m and n: node numbers in radial direction and circumferential direction, respectively.
- j and i: node indices in radial direction and circumferential direction, respectively.

The array of displacement vectors $\vec{\mathbf{u}}$ which contains the 2D displacement vectors of $m \cdot n$ nodes is defined as

$$\begin{aligned}\vec{\mathbf{u}} = \quad & [\vec{u}^{1,1}, \quad \vec{u}^{1,2}, \quad \ldots, \quad \vec{u}^{1,m}, \\ & \vec{u}^{2,1}, \quad \vec{u}^{2,2}, \quad \ldots, \quad \vec{u}^{2,m}, \\ & \cdots\cdots \\ & \vec{u}^{n,1}, \quad \vec{u}^{n,2}, \quad \ldots, \quad \vec{u}^{n,m}]^{\mathrm{T}}.\end{aligned} \tag{1}$$

The array of revised displacement vectors is defined in the same form as $\vec{\mathbf{u}}$, and its definition is

$$\vec{\mathbf{u}}' = \vec{\mathbf{u}} + \vec{\boldsymbol{\epsilon}}, \tag{2}$$

where $\vec{\boldsymbol{\epsilon}}$ is the array of displacement-revising vectors which also contains the 2D displacement-revising vector of $m \cdot n$ nodes. The array of displacement-revising vectors $\vec{\boldsymbol{\epsilon}}$ has the same definition form as eq. (1).

To obtain the displacement-revising vectors, an error function, which represents a balance between the revising effect and the compression or tension energy of the virtual springs, is defined. In the following function, the meanings of the parameters are listed below:

- $E_{\mathrm{rr}}^{i,j}$: pseudo elasticity parameter at node (i, j) that controls the displacement-revising effect in the radial direction.
- $E_{\mathrm{cc}}^{i,j}$: pseudo elasticity parameter at node (i, j) that controls the displacement-revising effect in the circumferential direction.
- $G_{\mathrm{rc}}^{i,j}$ and $G_{\mathrm{cr}}^{i,j}$: pseudo shear-elasticity parameters at node (i, j) that control the displacement-revising effects in the shear direction.

The error function is defined as

$$\begin{aligned} e(\boldsymbol{\epsilon}_{\mathrm{r}}, \boldsymbol{\epsilon}_{\mathrm{c}}) = & \sum_{i=1}^{n}\sum_{j=1}^{m}[(\epsilon_{\mathrm{r}}^{i,j})^2 + (\epsilon_{c}^{i,j})^2] \\ & + \sum_{i=1}^{n}\sum_{j=1}^{m-1}\frac{E_{\mathrm{rr}}^{i,j}}{2}(u_{\mathrm{r}}^{'i,j+1} - u_{\mathrm{r}}^{'i,j})^2 \\ & + \sum_{i=1}^{n-1}\sum_{j=1}^{m-1}\frac{G_{\mathrm{rc}}^{i,j}}{2}[(u_{\mathrm{r}}^{'i+1,j+1} - u_{\mathrm{r}}^{'i+1,j}) \\ & - (u_{\mathrm{r}}^{'i,j+1} - u_{\mathrm{r}}^{'i,j})]^2 \\ & + \sum_{i=1}^{n-1}\sum_{j=1}^{m}\frac{E_{\mathrm{cc}}^{i,j}}{2}(u_{\mathrm{c}}^{'i+1,j} - u_{\mathrm{c}}^{'i,j})^2 \\ & + \sum_{i=1}^{n-1}\sum_{j=1}^{m-1}\frac{G_{\mathrm{cr}}^{i,j}}{2}[(u_{\mathrm{c}}^{'i+1,j+1} - u_{\mathrm{c}}^{'i,j+1}) \\ & - (u_{\mathrm{c}}^{'i+1,j} - u_{\mathrm{c}}^{'i,j})]^2. \end{aligned} \tag{3}$$

When the error function is minimized, the displacement-revising vectors $\vec{\boldsymbol{\epsilon}}$ are considered to be optimal. By calculating all the partial derivatives of eq. (3) with respect to each element in $\boldsymbol{\epsilon}_{\mathrm{r}}$ and $\boldsymbol{\epsilon}_{\mathrm{c}}$, the following linear equations are obtained:

$$\frac{\partial e(\boldsymbol{\epsilon}_{\mathrm{r}}, \boldsymbol{\epsilon}_{\mathrm{c}})}{\partial \boldsymbol{\epsilon}_{\mathrm{r}}} = \mathbf{A}_{\mathrm{r}}\boldsymbol{\epsilon}_{\mathrm{r}} - \mathbf{b}_{\mathrm{r}} = 0, \tag{4}$$

$$\frac{\partial e(\boldsymbol{\epsilon}_{\mathrm{r}}, \boldsymbol{\epsilon}_{\mathrm{c}})}{\partial \boldsymbol{\epsilon}_{\mathrm{c}}} = \mathbf{A}_{\mathrm{c}}\boldsymbol{\epsilon}_{\mathrm{c}} - \mathbf{b}_{\mathrm{c}} = 0. \tag{5}$$

The detailed derivation process of $\mathbf{A}_{\mathrm{r}}$, $\mathbf{b}_{\mathrm{r}}$, $\mathbf{A}_{\mathrm{c}}$, and $\mathbf{b}_{\mathrm{c}}$ is described in the Appendix. The displacement-revising vectors $\boldsymbol{\epsilon}_{\mathrm{r}}$ and $\boldsymbol{\epsilon}_{\mathrm{c}}$ are calculated by solving the above linear eqs. (4) and (5). Finally, the array of revised displacement vectors is calculated by eq. (2).

The pseudo elasticity parameters $E_{\mathrm{rr}}^{i,j}$, $E_{\mathrm{cc}}^{i,j}$ and $E_{\mathrm{rc}}^{i,j}$ can be determined by the cross-correlation coefficients between two frame images pre- and post-deformation. This method is usually applied to displacement measurement, for example, STE. When the coefficients are high, the accuracy of the estimated displacements will also be high. Therefore the pseudo elasticity parameters can be mapped to high values when the coefficients are low, and to low values when the coefficients are high. The pseudo elasticity parameters can also be determined from the displacement error functions, which indicate the magnitude of the erroneous motion. The displacement error functions are defined as

$$\delta_{\mathrm{rr}}^{i,j} = \left|\frac{u_{\mathrm{r}}^{i,j+1} - 2u_{\mathrm{r}}^{i,j} + u_{\mathrm{r}}^{i,j-1}}{h_{\mathrm{r}}^{i,j} + h_{\mathrm{r}}^{i,j+1}}\right|, \tag{6}$$

$$\delta_{\mathrm{cc}}^{i,j} = \left|\frac{u_{\mathrm{c}}^{i+1,j} - 2u_{\mathrm{c}}^{i,j} + u_{\mathrm{c}}^{i-1,j}}{h_{\mathrm{c}}^{i,j} + h_{\mathrm{c}}^{i+1,j}}\right|, \tag{7}$$

$$\delta_{\mathrm{rc}}^{i,j} = \delta_{\mathrm{cr}}^{i,j} = \frac{\delta_{\mathrm{rr}}^{i,j} + \delta_{\mathrm{cc}}^{i,j}}{2}. \tag{8}$$

Here h_{r} and h_{c} are the distances between adjacent nodes in the radial and circumferential directions, respectively. These functions have a similar form to the discrete strain difference. If the difference is large, it means that the estimated displacement has a large error. Here we assume there are no rapid changes in the strain distribution. A simple way to map the displacement error functions to the pseudo elasticity parameters is to use linear functions, where the function values are mapped to a range $[E^{\min}, E^{\max}]$ based on the above displacement error functions. The definitions of the pseudo elasticity parameter functions are:

$$E_{\mathrm{rr}}^{i,j} = \frac{\delta_{\mathrm{rr}}^{i,j} - \delta_{\mathrm{rr}}^{\min}}{\delta_{\mathrm{rr}}^{\max} - \delta_{\mathrm{rr}}^{\min}}(E_{\mathrm{rr}}^{\max} - E_{\mathrm{rr}}^{\min}) + E_{\mathrm{rr}}^{\min}; \tag{9}$$

$$E_{\mathrm{cc}}^{i,j} = \frac{\delta_{\mathrm{cc}}^{i,j} - \delta_{\mathrm{cc}}^{\min}}{\delta_{\mathrm{cc}}^{\max} - \delta_{\mathrm{cc}}^{\min}}(E_{\mathrm{cc}}^{\max} - E_{\mathrm{cc}}^{\min}) + E_{\mathrm{cc}}^{\min}; \tag{10}$$

$$G_{\mathrm{rc}}^{i,j} = \frac{\delta_{\mathrm{rc}}^{i,j} - \delta_{\mathrm{rc}}^{\min}}{\delta_{\mathrm{rc}}^{\max} - \delta_{\mathrm{rc}}^{\min}}(G_{\mathrm{rc}}^{\max} - G_{\mathrm{rc}}^{\min}) + G_{\mathrm{rc}}^{\min}; \tag{11}$$

$$G_{\mathrm{cr}}^{i,j} = \frac{\delta_{\mathrm{cr}}^{i,j} - \delta_{\mathrm{cr}}^{\min}}{\delta_{\mathrm{cr}}^{\max} - \delta_{\mathrm{cr}}^{\min}}(G_{\mathrm{cr}}^{\max} - G_{\mathrm{cr}}^{\min}) + G_{\mathrm{cr}}^{\min}. \tag{12}$$

Here $\delta_{\mathrm{rr}}^{\min}$, $\delta_{\mathrm{cc}}^{\min}$, $\delta_{\mathrm{rc}}^{\min}$, and $\delta_{\mathrm{cr}}^{\min}$ are the detected minimal values from the displacement error function. Furthermore, $\delta_{\mathrm{rr}}^{\max}$, $\delta_{\mathrm{cc}}^{\max}$, $\delta_{\mathrm{rc}}^{\max}$, and $\delta_{\mathrm{cr}}^{\max}$ are the detected maximum values from the displacement error function. In this study, the optimized ranges of the pseudo elasticity parameters are manually selected from preliminary experiments by selecting different minimal and maximum pseudo elasticity parameters to give a good balance between spatial resolution and accuracy. In the preliminary experiments, different pseudo elasticity parameters are tested for obtaining smoothing effects. The minimal pseudo elasticity parameters are selected by making the smoothing effect only just observable, while the maximum pseudo elasticity parameters are selected by increasing the smoothing effect up to the point just before it becomes excessive. This method is used

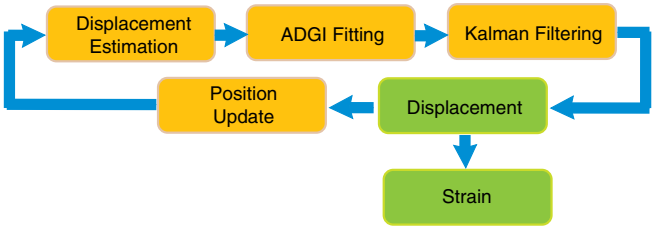

Fig. 2. (Color online) Displacement tracking and strain calculation process flow.

to determine the optimized pseudo elasticity parameter ranges in this study. Illustrations of the procedure are shown in §3.

In the current study, only the radial strain ε_{rr} is assessed. Therefore, only the radial displacement u_r is smoothed. To obtain a revised radial displacement u_r', only eq. (4) is solved. Because $\partial e(\boldsymbol{\epsilon}_r, \boldsymbol{\epsilon}_c)/\partial \boldsymbol{\epsilon}_r$ is only related to the parameters E_{rr} and G_{rc}, E_{cc} and G_{cr} are neglected in this study.

2.2 Displacement tracking and strain calculation

Generally, the correlation coefficient will be high when the scanning frame rate is high, and the accuracy of the estimated displacement will also be high. However unfortunately, the dynamic range of the displacement estimated from two consecutive frames will be low. Therefore, the strain calculation will be affected by the relatively high noise. In order to overcome this problem, a fixed-interval KF[24] is applied to position tracking, so that data from multiple frames can be tracked in the temporal dimension. The displacement data for each sampling node are first smoothed by ADGI, and then tracked by the KF. After each step, the positions of the grids are updated to estimate the displacement in the next step. The processing flow is illustrated in Fig. 2.

Displacement is generally defined by the difference between the positions at time steps k and $k-1$. The position vector $\mathbf{p}$ is related to the displacement vector $\mathbf{u}$ as

$$\mathbf{p}_k = \mathbf{p}_{k-1} + \mathbf{u}_{k-1}, \tag{13}$$

where the subscript k denotes the vector at time step k. In addition, the symbol $\mathbf{x}$ represents the internal state i.e. the position state. The KF can be described by two equations, the state equation and measurement equation as follows:

$$\begin{aligned} \mathbf{x}_k &= \mathbf{x}_{k-1} + \mathbf{n}_{k-1}, \\ \mathbf{p}_k &= \mathbf{x}_k + \mathbf{m}_k, \end{aligned} \tag{14}$$

where $\mathbf{n}_k$ is process noise and $\mathbf{m}_k$ is measurement noise, which are assumed to be independent, white, and with normal probability distributions.

The KF provides the closed-form recursive solution for the estimation of linear discrete-time dynamic systems, which can be described by equations of the form eq. (14). Detailed parameter estimation is discussed in refs. 24 and 25. Finally, the mean position vector $\hat{\mathbf{p}}_k$ is estimated, and then the accumulated strain data are calculated by[26]

$$\boldsymbol{\varepsilon}_{rr,k} = \frac{\partial(\hat{\mathbf{p}}_k - \mathbf{p}_0)_r}{\partial \mathbf{r}}, \tag{15}$$

where $\mathbf{p}_0$ is the initial position and r is the displacement component in radial direction.

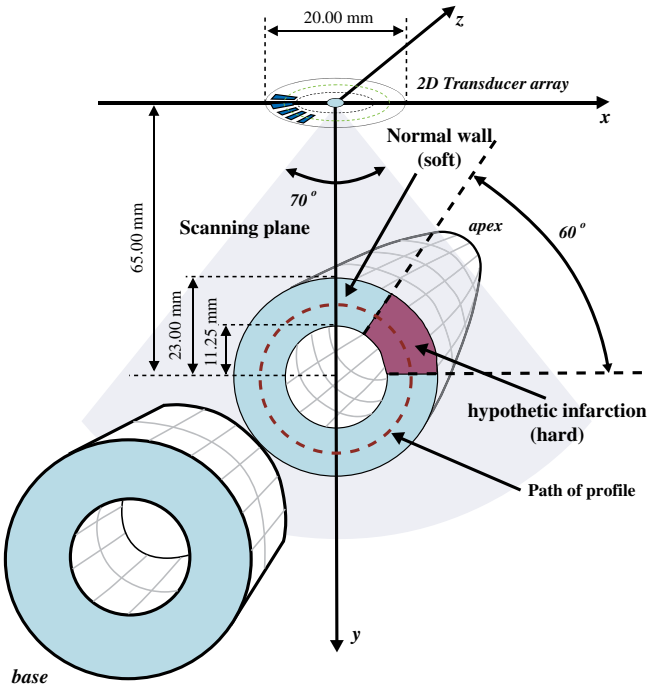

Fig. 3. (Color online) Illustration of the measuring conditions (model 2), scanning plane, and the path of the profile.

3. Simulation Analysis

3D myocardial strain-imaging performance is evaluated by numerically simulating the short-axis imaging of a 3D myocardial model, as illustrated in Fig. 3. A digital LV phantom is used for generating the LV shape before and after deformation. The endocardium radius is 11.25 mm and the epicardium radius is 23 mm. The strain curve used in the simulation is shown in Fig. 4(a), and the displacement curve is shown in Fig. 4(b). The stiffness of the infarction is set to be about three times that of the surrounding normal wall, because this stiffness ratio is generally referred to as the typical stiffness ratio of the infarction to the normal wall.[7] To achieve a stiffness in the infarcted region three times that in the normal region, the radial strain ε_{rr} in the infarcted region is set to be one-third of that in the normal region.

Applying these parameters of the simulation model to each mesh node in the LV model, post deformation models are constructed. In the normal wall, the radial strain is set to be ε, while in the infarcted wall the radial strain is set to be $\varepsilon/3$. For each mesh node, the first step is detecting whether or not the node is located in the infarcted region. After that, the displacement vector is calculated using the determined radial strain. In this simulation model, the radial displacement in the infarcted wall is one-third of that in the normal wall. By combining the original position with the calculated displacement, the new position can be obtained. For the profile in the circumferential direction, the strain distribution is approximately a square wave. The myocardium is frequently considered an incompressible body, and myocardial motion consists of displacements due to deformation and translation.[7] Therefore, the positions of the scatterers are relocated according to the post deformation results. Next, the simulated RF signals are generated from the scatterer field.

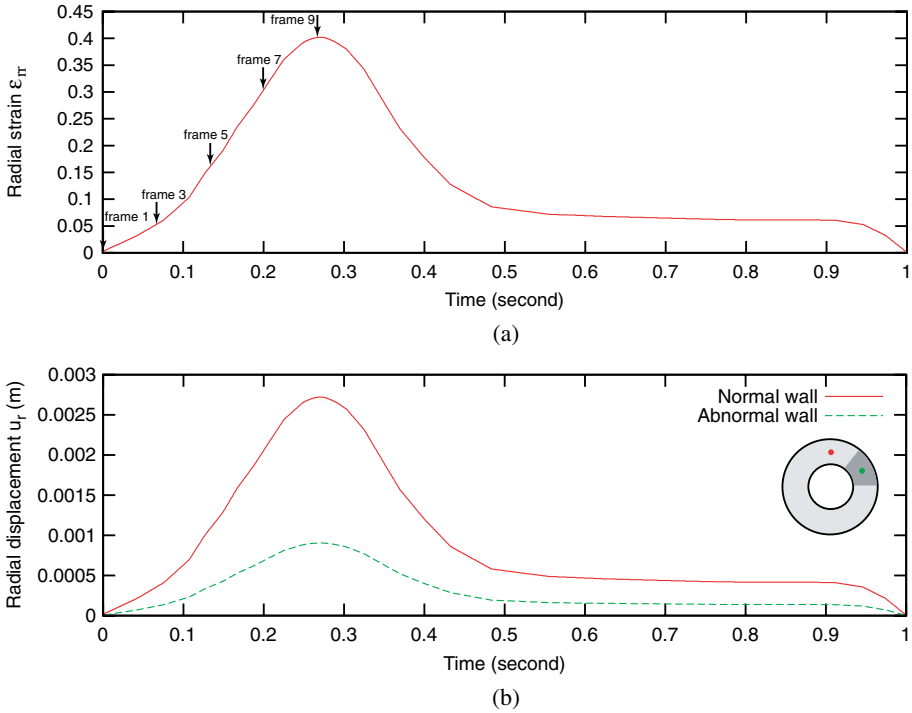

Fig. 4. (Color online) (a) Radial strain curve and (b) radial displacement curve of a cardiac cycle.

The external diameter of the 2D transducer is 20 mm. The ultrasonic pulse has a center frequency of 3.75 MHz and the fractional bandwidth is 40%. The scanning plane is located midway between the apex and the base when viewed from the short-axis. The scanning plane and hypothetical infarction are illustrated in Fig. 3. The scanning frame rate is 30 FPS. In these simulations, RF signals with a signal-to-noise ratio (SNR) of 20 dB are digitized at a rate of 20 MHz. The moving-average-filter window is $W_a = 3.5$ mm, the same size as that used in our previous studies.[27–29] The numbers of elements in the radial and circumferential directions are 80 and 256, respectively. The optimized pseudo elasticity parameters are set in the range of 20 to 2800 in the radial direction and 20 to 800 in the shear direction from the results of preliminary experiments as mentioned in §2.1. The optimized pseudo elasticity parameter ranges are determined by using the data for one frame generated from the same simulation model. The images and profiles illustrating the selection of the minimum and maximum pseudo elasticity parameters are shown in Fig. 5. In the preliminary experiments, the radial strain is set to be 4%, which is the averaged strain value between frames 1 and 9. Figure 5(a) is the resulting image obtained using the optimized pseudo elasticity parameter ranges, (b) is the resulting image when the smoothing effect is insufficient, (c) is the resulting image when the smoothing effect is excessive, and (d) shows the profiles of figures (a)–(c).

To evaluate angle dependence of the proposed method, two models with different infarction positions are simulated. In model 1, the infarcted wall is located at approximately 5 to 7 o'clock, where its radial motion and that of the ultrasound beam are identical. Under this condition, the motion of the abnormal wall can be detected by both TDI and SRI. In model 2, the infarcted wall is located at approximately 1 to 3 o'clock. Neither TDI nor SRI can accurately detect the wall motion in this region.[1–4]

The resulting images obtained from model 1 are shown in Fig. 6. Figures 6(a1)–6(a5) show the radial strain generated by using the moving average filter at frames 1, 3, 5, 7, and 9, respectively. Figures 6(b1)–6(b5) show the radial strain generated by the proposed method at frames 1, 3, 5, 7, and 9, respectively. Figures 6(c1)–6(c5) show the radial strain generated by the proposed method without adding noise at frames 1, 3, 5, 7, and 9, respectively. The radial strain profiles are shown in Fig. 6(d). The corresponding results for model 2 are shown in Fig. 7.

From the resulting images, we can see that our proposed method does not have the problem of angle dependence. There are no instances of a distinct decrease in accuracy in model 2 in contrast with model 1. In both models, although the noise level is high, the strain data calculated from the accumulated displacement have better accuracy and stability.

4. Discussion

For ultrasound myocardial strain imaging, the angle dependence and strain calculation are two major problems that have still not been resolved perfectly. Angle dependence is limited by the nature of ultrasound. Using our previously proposed WPG method, full displacement vectors can be detected with a 2D array transducer. The problem of strain calculation is caused by the amplification of displacement noise in strain images. A novel displacement-fitting method, ADGI has been proposed for overcoming these problems. With the adaptive pseudo elasticity parameter selection, the fitting or smoothing effect can be adjusted automatically,

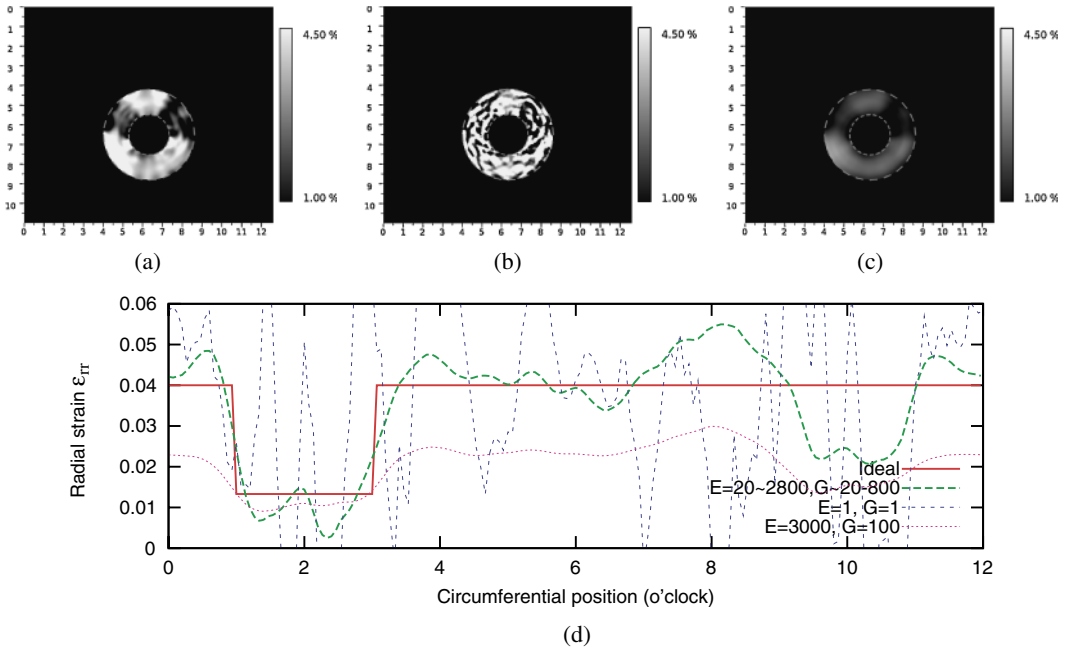

Fig. 5. (Color online) Images and profiles of radial strain used for determining the ranges of pseudo elasticity parameters: (a) $E = 20-2800$, $G = 20-800$; (b) $E = 1$, $G = 1$, (c) $E = 3000$, $G = 1000$, and (d) profiles corresponding to minimum and maximum parameters. The length unit in the above figures is cm.

obtaining better smoothing performance. By tracking myocardial motion and calculating the strain from the accumulated displacement, the accuracy and stability can be further improved.

In the strain calculation, because the adjacent sampling node distance is typically small and the differential operator is extremely sensitive to noise, a small fluctuation in displacement can produce a larger fluctuation in the result for strain. This problem can be approximately resolved by increasing the step size in the calculation of displacement differential, but this produces low spatial resolution in the strain images. The proposed ADGI method does not include the concept of window size; the smoothing is performed by solving a global error function to find the displacement-revising vectors. If the noise level is high in some region, the pseudo elasticity parameters are set to be large; in addition, the virtual springs pull the node back. In the error function, the first term represents the revising effect, and the second term represents the compression or tension energy of the virtual springs. If the overall revising effect is large, the compression or tension energy of virtual springs will be small. On the other hand, if the overall revising effect is small, the displacements among the nodes are disordered, and the compression or tension energy of the virtual springs is large. When the error function is minimized, the revising effect and compression or tension energy of the virtual springs is balanced. The pseudo elasticity parameters control the balance between these two items. When the pseudo elasticity parameters are large, the virtual spring is stiff, greatly restricting erroneous motion. If the noise level in a region is small, the pseudo elasticity parameters can be set to small values; consequently, the virtual spring is soft and the smoothing effect is small. Therefore, the smoothing effect is globally optimized, and a good balance between spatial resolution and accuracy can be achieved. Unlike the median and moving-average filters, there are mechanical considerations in this method; thus, the fitting results are more meaningful.

Although the proposed method can output better results, it also has a drawback: the processing is complex and a large amount of computational resources is needed. The complexity of ADGI is $O[(nm)^3]$, where n and m denote the mesh sizes. If the window sizes are w_1 and w_2, the complexity of the moving average filter is $O(nmw_1w_2)$, and the complexity of the median filter is $O[nmw_1w_2\log(w_1w_2)]$. The computation time is greatly increased with increasing mesh sizes. This problem can be resolved by dividing the mesh into several overlapping meshes. However with the rapid development of computer hardware, this problem is not critical.

The ranges of the optimized pseudo elasticity parameters are manually selected in this study. However in real measurement environments, it is difficult to obtain real strain data. In addition, differences in the mesh size, the distance between adjacent nodes, the amplitude of displacement, and the noise level will affect the parameter selection. For a different model, the optimized pseudo elasticity parameters ranges will be different. Therefore a more reliable parameter selection method is important and will be researched in a future study.

In the error function defined as eq. (3), the differences of myocardial stiffness at different positions are not considered. However, the contraction of a normal wall is usually larger than that of an abnormal wall. Therefore, using the same pseudo elasticity parameter ranges adjusted for a normal wall, the fitting in the abnormal wall may be excessive in some cases. In this study, to simplify the implementation, this effect is neglected. In a future work, the stiffness of the myocardium itself will be considered, and iterative processing will be used to obtain a better fitting result for the whole area of the myocardium.

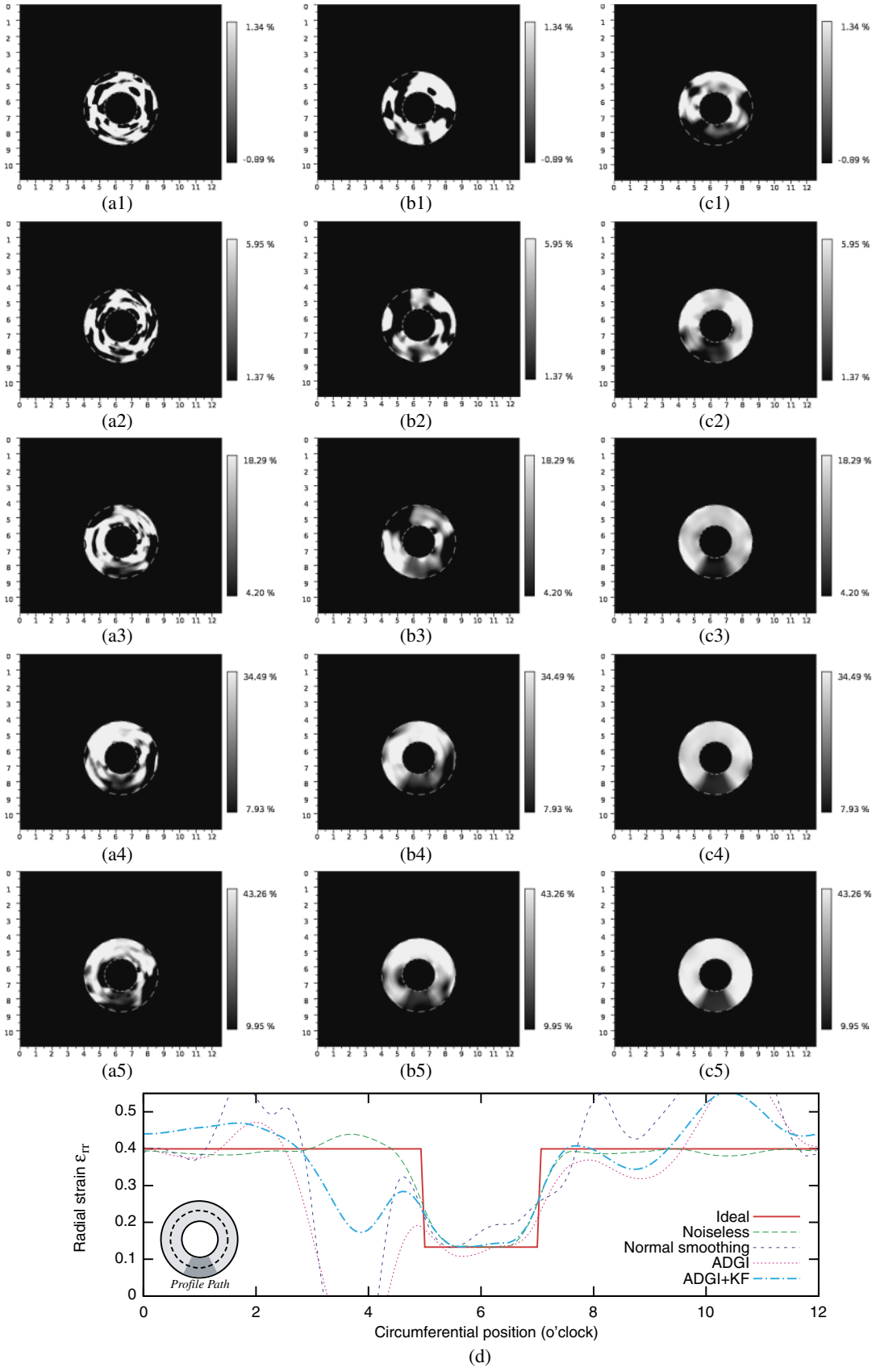

Fig. 6. (Color online) Resulting images and profiles of radial stain for model 1: (a1) frame 1, normal smoothing, (a2) frame 3, normal smoothing, (a3) frame 5, normal smoothing, (a4) frame 7, normal smoothing, (a5) frame 9, normal smoothing, (b1) frame 1, ADGI+KF, (b2) frame 3, ADGI+KF, (b3) frame 5, ADGI+KF, (b4) frame 7, ADGI+KF, (b5) frame 9, ADGI+KF, (c1) frame 1, ADGI+KF, noiseless, (c2) frame 3, ADGI+KF, noiseless, (c3) frame 5, ADGI+KF, noiseless, (c4) frame 7, ADGI+KF, noiseless, (c5) frame 9, ADGI+KF, noiseless, and (d) profiles, frame 9. The length unit is cm.

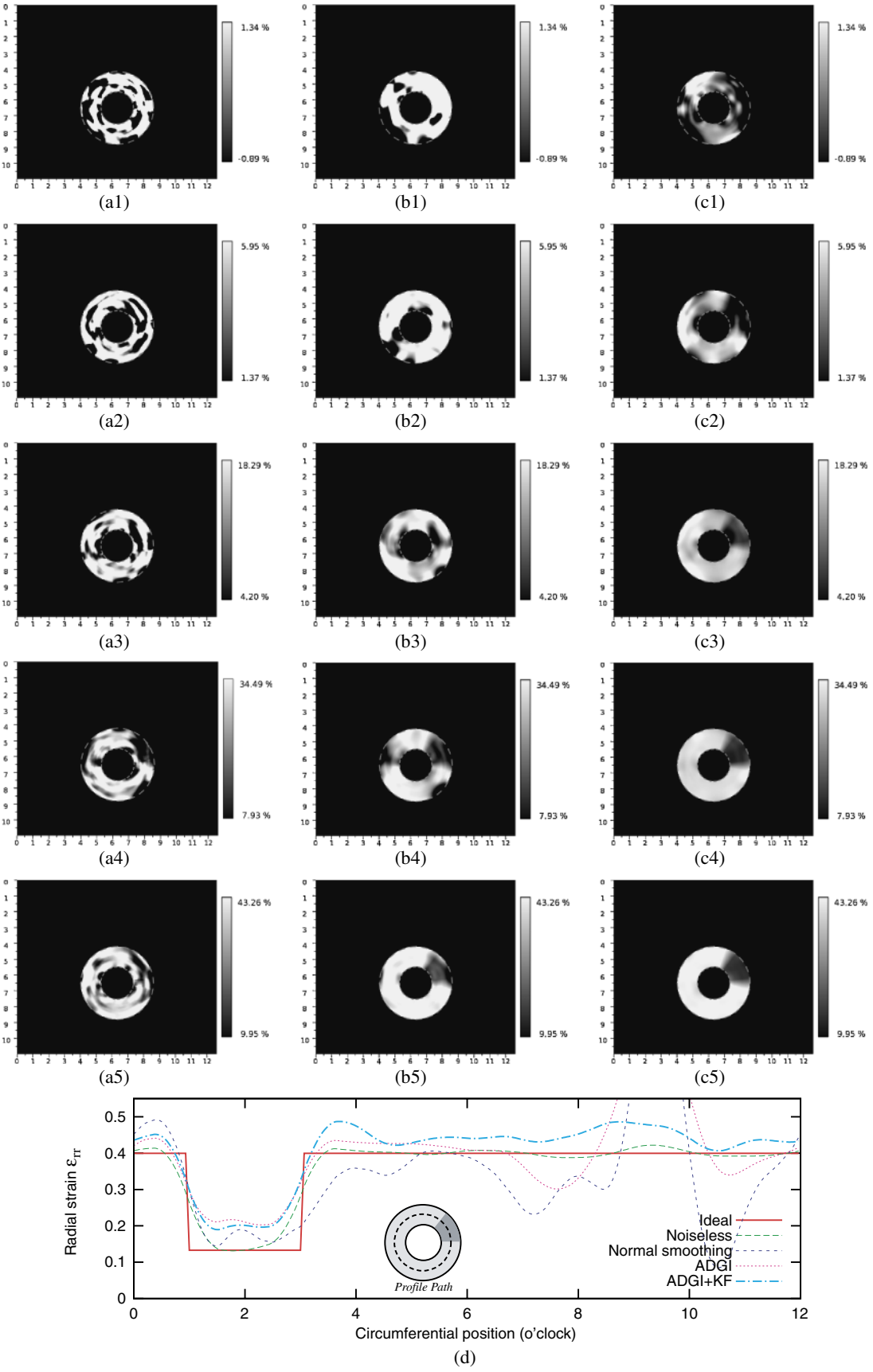

Fig. 7. (Color online) Resulting images and profiles of radial strain for model 2: (a1) frame 1, normal smoothing, (a2) frame 3, normal smoothing, (a3) frame 5, normal smoothing, (a4) frame 7, normal smoothing, (a5) frame 9, normal smoothing, (b1) frame 1, ADGI+KF, (b2) frame 3, ADGI+KF, (b3) frame 5, ADGI+KF, (b4) frame 7, ADGI+KF, (b5) frame 9, ADGI+KF, (c1) frame 1, ADGI+KF, noiseless, (c2) frame 3, ADGI+KF, noiseless, (c3) frame 5, ADGI+KF, noiseless, (c4) frame 7, ADGI+KF, noiseless, (c5) frame 9, ADGI+KF, noiseless, and (d) profiles, frame 9. The length unit is cm.

5. Conclusions

In this paper, a novel displacement-fitting method ADGI is presented. Because its fitting or smoothing effect can be automatically adjusted on the basis of the noise level, it provides stable and accurate myocardial strain images with high spatial resolution. By utilizing myocardial motion tracking and calculating the strain from the accumulated displacement, further improvements are also obtained. From the simulation results, we can conclude that the images generated by the proposed method are accurate, robust, and have high spatial resolution. Therefore, the proposed method is expected to provide more accurate diagnostic information.

1) W. M. McDicken, G. R. Sutherland, C. M. Moran, and L. N. Gordon: Ultrasound Med. Biol. **18** (1992) 651.
2) N. Yamazaki, Y. Mine, A. Sano, M. Hirama, K. Miyatake, M. Yamagishi, and N. Tanaka: Jpn. J. Appl. Phys. **33** (1994) 3141.
3) G. R. Sutherland, M. J. Stewart, and K. W. E. Groundstroem: J. Am. Soc. Echocardiography **7** (1994) 441.
4) T. Edvardsen, S. Urheim, H. Skulstad, K. Steine, H. Ihlen, and O. A. Smiseth: Circulation **105** (2002) 2071.
5) A. Heimdal, A. Stoyle, H. Torp, and T. Skjaerpe: J. Am. Soc. Echocardiography **11** (1998) 1013.
6) J. D'hooge, E. Konofagou, F. Jamal, A. Heimdal, L. Barrios, B. Bijnens, J. Thoen, F. Van de Werf, G. Sutherland, and P. Suetens: IEEE Trans. Ultrason. Ferroelectr. Freq. Control **49** (2002) 281.
7) K. Kaluzynski, X. Chen, S. Y. Emelianov, A. R. Skovoroda, and M. O'Donnell: IEEE Trans. Ultrason. Ferroelectr. Freq. Control **48** (2001) 1111.
8) P. L. Castro, N. L. Greenberg, J. Drinko, M. J. Garcia, and J. D. Thomas: Biomed. Sci. Instrum. **36** (2000) 197.
9) X. Papademetris, A. J. Sinusas, D. P. Dione, and J. S. Duncan: Med. Image Anal. **5** (2001) 17.
10) L. N. Bohs and G. E. Trahey: IEEE Trans. Biomed. Eng. **38** (1991) 280.
11) J. Meunier and M. Bertrand: IEEE Trans. Med. Imaging **14** (1995) 293.
12) L. N. Bohs, B. Geiman, M. Anderson, S. Gebhart, and G. E. Trahey: Ultrasonics **38** (2000) 369.
13) T. Shiina, K. Kondo, and M. Yamakawa: IEEE Ultrasonics Symp., 2009, p. 2284.
14) C. Sumi and A. Tanuma: Jpn. J. Appl. Phys. **47** (2008) 4137.
15) S. Bu, T. Shiina, M. Yamakawa, and H. Takizawa: IEEJ Trans. Electron. Inf. Syst. **127** (2007) 1732.
16) M. Yamakawa, S. Bu, and T. Shiina: IEEE Ultrasonics Symp., 2008, p. 2021.
17) T. Shiina, M. M. Doyel, and J. C. Bamber: IEEE Ultrasonics Symp., 1996, p. 1331.
18) M. Yamakawa and T. Shiina: Jpn. J. Appl. Phys. **40** (2001) 3872.
19) M. Yamakawa, N. Nitta, T. Shiina, T. Matsumura, S. Tamano, T. Mitake, and E. Ueno: Jpn. J. Appl. Phys. **42** (2003) 3265.
20) N. Nitta and T. Shiina: Jpn. J. Appl. Phys. **37** (1998) 3058.
21) N. Nitta and T. Shiina: Jpn. J. Appl. Phys. **39** (2000) 3225.
22) T. Kinugawa, H. Hasegawa, and H. Kanai: Jpn. J. Appl. Phys. **47** (2008) 4155.
23) W. H. Press, S. A. Teukolsky, W. T. Vetterling, and B. P. Flannery: *Numerical Recipes in C* (Cambridge University Press, New York, 1992).
24) Y. Bar-Shalom, X. R. Li, and T. Kirubaraan: *Estimation with Applications to Tracking and Navigation* (Wiley, New York, 2001).
25) G. Welch and G. Bishop: An Introduction to the Kalman Filter (SIGGRAPH 2001, course 8).
26) Y. C. Fung: *A First Course in Continuum Mechanics* (Prentice-Hall, Upper Saddle River, NJ, 1993).
27) N. Nitta, M. Yamakawa, and T. Shiina: 24th Symp. Ultrasonic Electronics, 2003, p. 337.
28) N. Nitta and T. Shiina: IEEE Ultrasonics Symp., 2003, p. 1258.
29) N. Nitta and T. Shiina: Jpn. J. Appl. Phys. **43** (2004) 3249.
30) E. Anderson, Z. Bai, C. Bischof, S. Blackford, J. Demmel, J. Dongarra, J. D. Croz, A. Greenbaum, S. Hammarling, A. McKenney, and D. Sorensen: *LAPACK Users' Guide* (Society for Industrial and Applied Mathematics, Philadelphia, PA, 1999) 3rd ed.

Appendix: Matrix Definition and Implementation

In the implementation, a matrix form is used. Herein, the 2D index (i, j) in eq. (3) is converted to the 1D index $(i-1)m+j$. Substituting eq. (2) into eq. (3), and then expanding it, the following formula is obtained:

$$
\begin{aligned}
e(\boldsymbol{\epsilon}_{\mathrm{r}}, \boldsymbol{\epsilon}_{\mathrm{c}}) = {} & (\epsilon_{\mathrm{r}}^{1})^2 + \frac{E_{\mathrm{rr}}^{1}}{2}(u_{\mathrm{r}}^{2} + \epsilon_{\mathrm{r}}^{2} - u_{\mathrm{r}}^{1} - \epsilon_{\mathrm{r}}^{1})^2 \\
& + \frac{G_{\mathrm{rc}}^{1}}{2}(u_{\mathrm{r}}^{m+2} + \epsilon_{\mathrm{r}}^{m+2} - u_{\mathrm{r}}^{m+1} - \epsilon_{\mathrm{r}}^{m+1} - u_{\mathrm{r}}^{2} - \epsilon_{\mathrm{r}}^{2} + u_{\mathrm{r}}^{1} - \epsilon_{\mathrm{r}}^{1})^2 \\
& + \cdots \\
& + (\epsilon_{\mathrm{r}}^{(i-1)m+j})^2 + \frac{E_{\mathrm{rr}}^{(i-1)m+j}}{2}(u_{\mathrm{r}}^{(i-1)m+j+1} + \epsilon_{\mathrm{r}}^{(i-1)m+j+1} - u_{\mathrm{r}}^{(i-1)m+j} - \epsilon_{\mathrm{r}}^{(i-1)m+j})^2 \\
& + \frac{G_{\mathrm{rc}}^{(i-1)m+j}}{2}(u_{\mathrm{r}}^{im+j+1} + \epsilon_{\mathrm{r}}^{im+j+1} - u_{\mathrm{r}}^{im+j} - \epsilon_{\mathrm{r}}^{im+j} \\
& \quad - u_{\mathrm{r}}^{(i-1)m+j+1} - \epsilon_{\mathrm{r}}^{(i-1)m+j+1} + u_{\mathrm{r}}^{(i-1)m+j} + \epsilon_{\mathrm{r}}^{(i-1)m+j})^2 \\
& + \cdots \\
& + (\epsilon_{\mathrm{c}}^{1})^2 + \frac{E_{\mathrm{cc}}^{1}}{2}(u_{\mathrm{c}}^{m+1} + \epsilon_{\mathrm{c}}^{m+1} - u_{\mathrm{c}}^{1} - \epsilon_{\mathrm{c}}^{1})^2 \\
& + \frac{G_{\mathrm{cr}}^{1}}{2}(u_{\mathrm{c}}^{m+2} + \epsilon_{\mathrm{c}}^{m+2} - u_{\mathrm{c}}^{2} - \epsilon_{\mathrm{c}}^{2} - u_{\mathrm{c}}^{m+1} - \epsilon_{\mathrm{c}}^{m+1} + u_{\mathrm{c}}^{1} + \epsilon_{\mathrm{c}}^{1})^2 \\
& + \cdots \\
& + (\epsilon_{\mathrm{c}}^{(i-1)m+j})^2 + \frac{E_{\mathrm{cc}}^{(i-1)m+j}}{2}(u_{\mathrm{c}}^{im+j} + \epsilon_{\mathrm{c}}^{im+j} - u_{\mathrm{c}}^{(i-1)m+j} - \epsilon_{\mathrm{c}}^{(i-1)m+j})^2 \\
& + \frac{G_{\mathrm{cr}}^{(i-1)m+j}}{2}(u_{\mathrm{c}}^{im+j+1} + \epsilon_{\mathrm{c}}^{im+j+1} - u_{\mathrm{c}}^{(i-1)m+j+1} - \epsilon_{\mathrm{c}}^{(i-1)m+j+1} \\
& \quad - u_{\mathrm{c}}^{im+j} - \epsilon_{\mathrm{c}}^{im+j} + u_{\mathrm{c}}^{(i-1)m+j} + \epsilon_{\mathrm{c}}^{(i-1)m+j})^2 \\
& + \cdots . \qquad \text{(A·1)}
\end{aligned}
$$

When the error function is minimized, the displacement-revising vectors $\vec{\epsilon}$ are considered to be optimal. In order to obtain the displacement-revising vectors, the partial derivatives of eq. (A·1) with respect to each element in $\boldsymbol{\epsilon}_r$ and $\boldsymbol{\epsilon}_c$ are calculated. For example, at node (i, j) the equation that contains the partial derivative $\partial e(\boldsymbol{\epsilon}_r, \boldsymbol{\epsilon}_c)/\partial \epsilon_r^{(i-1)m+j}$ is

$$\begin{aligned}
0 = {} & 2\epsilon_r^{(i-1)m+j} \\
& - E_{rr}^{(i-1)m+j}(u_r^{(i-1)m+j+1} + \epsilon_r^{(i-1)m+j+1} - u_r^{(i-1)m+j} - \epsilon_r^{(i-1)m+j}) \\
& + E_{rr}^{(i-1)m+j-1}(u_r^{(i-1)m+j} + \epsilon_r^{(i-1)m+j} - u_r^{(i-1)m+j-1} - \epsilon_r^{(i-1)m+j-1}) \\
& + G_{rc}^{(i-1)m+j}(u_r^{im+j+1} + \epsilon_r^{im+j+1} - u_r^{im+j} - \epsilon_r^{im+j} \\
& \quad - u_r^{(i-1)m+j+1} - \epsilon_r^{(i-1)m+j+1} + u_r^{(i-1)m+j} + \epsilon_r^{(i-1)m+j}) \\
& + G_{rc}^{(i-2)m+j-1}(u_r^{(i-1)m+j} + \epsilon_r^{(i-1)m+j} - u_r^{(i-1)m+j-1} - \epsilon_r^{(i-1)m+j-1} \\
& \quad - u_r^{(i-2)m+j} - \epsilon_r^{(i-2)m+j} + u_r^{(i-2)m+j-1} + \epsilon_r^{(i-2)m+j-1}) \\
& - G_{rc}^{(i-2)m+j}(u_r^{(i-1)m+j+1} + \epsilon_r^{(i-1)m+j+1} - u_r^{(i-1)m+j} - \epsilon_r^{(i-1)m+j} \\
& \quad - u_r^{(i-2)m+j+1} - \epsilon_r^{(i-2)m+j+1} + u_r^{(i-2)m+j} + \epsilon_r^{(i-2)m+j}) \\
& - G_{rc}^{(i-1)m+j-1}(u_r^{im+j} + \epsilon_r^{im+j} - u_r^{im+j-1} - \epsilon_r^{im+j-1} \\
& \quad - u_r^{(i-1)m+j} - \epsilon_r^{(i-1)m+j} + u_r^{(i-1)m+j-1} + \epsilon_r^{(i-1)m+j-1}).
\end{aligned} \tag{A·2}$$

Rearranging and sorting the above equation, the following simplified equation can be obtained:

$$\begin{aligned}
& \epsilon_r^{(i-2)m+j-1}(G_{rc}^{(i-2)m+j-1}) + \epsilon_r^{(i-2)m+j}(-G_{rc}^{(i-2)m+j-1} - G_{rc}^{(i-2)m+j}) + \epsilon_r^{(i-2)m+j+1}(G_{rc}^{(i-2)m+j}) \\
& \quad + \epsilon_r^{(i-1)m+j-1}(-E_{rr}^{(i-1)m+j-1} - G_{rc}^{(i-2)m+j-1} - G_{rc}^{(i-1)m+j-1}) \\
& \quad + \epsilon_r^{(i-1)m+j}(2 + E_{rr}^{(i-1)m+j} + E_{rr}^{(i-1)m+j-1} + G_{rc}^{(i-1)m+j} + G_{rc}^{(i-2)m+j-1} + G_{rc}^{(i-2)m+j} + G_{rc}^{(i-1)m+j-1}) \\
& \quad + \epsilon_r^{(i-1)m+j+1}(-E_{rr}^{(i-1)m+j} - G_{rc}^{(i-1)m+j} - G_{rc}^{(i-2)m+j}) \\
& \quad + \epsilon_r^{im+j-1}(G_{rc}^{(i-1)m+j-1}) + \epsilon_r^{im+j}(-G_{rc}^{(i-1)m+j} - G_{rc}^{(i-1)m+j-1}) + \epsilon_r^{im+j+1}(G_{rc}^{(i-1)m+j}) \\
& = + E_{rr}^{(i-1)m+j}(u_r^{(i-1)m+j+1} - u_r^{(i-1)m+j}) - E_{rr}^{(i-1)m+j-1}(u_r^{(i-1)m+j} - u_r^{(i-1)m+j-1}) \\
& \quad - G_{rc}^{(i-1)m+j}(u_r^{im+j+1} - u_r^{im+j} - u_r^{(i-1)m+j+1} + u_r^{(i-1)m+j}) \\
& \quad - G_{rc}^{(i-2)m+j-1}(u_r^{(i-1)m+j} - u_r^{(i-1)m+j-1} - u_r^{(i-2)m+j} + u_r^{(i-2)m+j-1}) \\
& \quad + G_{rc}^{(i-2)m+j}(u_r^{(i-1)m+j+1} - u_r^{(i-1)m+j} - u_r^{(i-2)m+j+1} + u_r^{(i-2)m+j}) \\
& \quad + G_{rc}^{(i-1)m+j-1}(u_r^{im+j} - u_r^{im+j-1} - u_r^{(i-1)m+j} + u_r^{(i-1)m+j-1}).
\end{aligned} \tag{A·3}$$

In this equation, the left part contains the elements of matrix $\mathbf{A}_r$ in the $[(i-1)m+j]$-th row. The column indices of the elements are: $(i-2)m+j-1$, $(i-2)m+j$, $(i-2)m+j+1$, $(i-1)m+j-1$, $(i-1)m+j$, $(i-1)m+j+1$, $im+j-1$, $im+j$, and $im+j+1$. The right part of (A·3) is the corresponding element of array $\mathbf{b}_r$ in the same row. After calculating the partial derivatives of all $m \cdot n$ nodes, the sparse matrix $\mathbf{A}_r$ and array $\mathbf{b}_r$ can be determined. In the same way, matrix $\mathbf{A}_c$ and array $\mathbf{b}_c$ can also be determined. The linear equations given by eqs. (4) and (5) can be solved by using QR factorization.[23] Because the number of linear equations is very large, LAPACK[30] is used for solving them.